Journal of Applied Fluid Mechanics, Vol. 15, No. 5, pp. 1621-1634, 2022.
Available online at www.jafmonline.net, ISSN 1735-3572, EISSN 1735-3645.
https://doi.org/10.47176/jafm.15.05.1190

Physical Reasoning of Double- to Single-Loop Transition in Industrial Reactors using Computational Fluid Dynamics

D. K. Iyer[1] and A. K. Patel[2†]

[1] *National Institute of Technology Warangal 1, Warangal, Telangana, 506004, India*
[2] *National Institute of Technology Warangal 2, Warangal, Telangana, 506004, India*

†*Corresponding Author Email: akpcivil@nitw.ac.in*

(Received March 17, 2022; accepted June 5, 2022)

ABSTRACT

Double- to single-loop pattern transition and a significant reduction in the power number with a decrease in the clearance of the Rushton turbine impeller in a baffled reactor was elucidated in earlier research works. The present work investigates the physical reasons behind these phenomena using the computational fluid dynamics approach. The Reynolds Averaged Navier–Stokes equations with standard $k-\varepsilon$ turbulence model closure were used to model the turbulent flow conditions in the reactor vessels. The Multiple Reference Frame (MRF) approach was adopted to model the impeller baffle interactions in the reactor vessels. The implicit Volume of Fluid (VOF) method was employed to simulate the aeration process in the reactor configurations considered. The development of a low pressure region below the impeller of a low clearance vessel deflects the discharge streams downward, leading to the formation of a single-loop pattern. The downward movement of the discharge streams reduces the vortex activity behind the impeller blades, leading to weaker form drag and a decrease in the power number of the impeller. Similarly, a high clearance vessel provides a low pressure region above the impeller which deflects the discharge streams above the impeller, resulting in a single-loop pattern and a considerable increase in the air entrainment due to superior vortex and turbulence activity present near the free liquid surface. The standard reactor vessel was found to provide superior bulk mixing of fluid as the overall turbulent dissipation rate is 35% more than that associated with low and high clearance vessels.

Keywords: Flow patterns; Low clearance vessel; Mixing; Power number; RANS model; Stirred vessel; Turbulence.

NOMENCLATURE

B	width of baffle walls	$N_{p\varepsilon}$	power number based on volume integrated turbulence dissipation rate
b	width of blade	P	pressure
C_p	coefficient of pressure	P'	power drawn by the impeller
D	impeller diameter	Re	Reynolds number
d	vessel diameter	s	euclidean norm of strain rate tensor
e	gas hold-up	T	impeller torque
H	height of liquid	u_r	radial velocity
H_d	height of liquid during surface aeration	u_{tip}	impeller tip velocity
h	impeller clearance	w	euclidean norm of rotation rate tensor
k	turbulent kinetic energy	ε	turbulent dissipation rate
l	length of blade	ρ	density of fluid
N	impeller speed		
N_{pt}	power number based on impeller torque		

1. INTRODUCTION

Mechanically-agitated reactor vessels are widely used for the mixing and mass transfer processes associated with the chemical, pharmaceutical, petroleum, mineral and metallurgical industries (Li *et al.* 2020). The Rushton Turbine (RT) impeller is widely employed for agitation purposes in those

industries (Debab *et al.* 2011). The performance of the reactor vessels needs to be enhanced to achieve necessary performance objectives with minimum financial losses (Joshi *et al.* 2011). The optimal performance of the reactor vessel can be obtained by careful selection of the underlying geometric and operating parameters (Joshi *et al.* 2011). The proper configuration of the reactor vessel in turn develops flow conditions suitable for the various physical and chemical processes related to the reactor vessel.

Computational Fluid Dynamics (CFD) has been widely employed for modeling flow and transport processes in mechanically-agitated reactors (Li *et al.* 2020). The local velocity and turbulence characteristics obtained from the CFD models can be effectively used for selecting the optimal configuration of the reactor vessels (Zamiri and Chunk 2018). Moreover, CFD modeling provides flow field results within a short period of time and alleviates the need for extensive experiments to achieve the same results (Coroneo *et al.* 2011).

Impeller clearance (distance of the RT impeller from the bottom surface of the vessel) is a critical geometric parameter which significantly affects the flow patterns and performance goals associated with reactor vessels (Nienow 1968). The standard configuration of a reactor vessel with an RT impeller at one-third the height of the tank develops strong discharge streams which move radially outward from the impeller blades and strike on the tank periphery to provide a double re-circulation pattern (Yianneskis *et al.* 1987). Details regarding the discharge streams, periodic trailing vortices and random turbulent fluctuations were studied by various researchers such as Wu and Patterson (1989), Lee and Yianneskis (1998), Escudie and Line (2003), Escudie *et al.* 2004) and Yapici *et al.* (2008). Moreover, significant transfer of turbulent kinetic energy occurs from mean discharge streams to periodic trailing vortices and random turbulence fluctuations, leading to superior bulk mixing of the fluid contained within the reactor vessel (Escudie and Line 2003).

On the other hand, an RT impeller located near the bottom surface of the reactor vessel (low clearance vessel) generates axial discharge streams which strike on the bottom surface of the vessel to develop a single re-circulation pattern. The features of a down-pumping single-loop pattern such as axial velocity magnitudes, angle of inclination of discharge streams and secondary vortices below the impeller and near the free liquid surface were analyzed by various scholars such as Montante *et al.* (1999, 2001b), Ochieng *et al.* (2008), Li *et al.* (2011) and Zhu *et al.* (2019). Substantial energy transfer occurs from the impeller region to the bottom surface of the vessel as the discharge streams and the allied trailing vortices are pumped downward to the bottom surface of the reactor vessel (Li *et al.* 2011). The increase in the vortex and turbulent activity near the bottom surface of the reactor vessel helps in lifting the solid particles off the bottom surface of the vessel, resulting in proper suspension of the same in the liquid contained within the reactor vessel (Montante *et al.* 1999). The RT impeller placed near the free liquid surface (high clearance vessel) also develops axial discharge streams which are inclined toward the free liquid surface, leading to the formation of an up-pumping single re-circulation pattern. The characteristics of these up-pumping single-loop patterns such as angle of inclination of discharge streams, wave action near the free liquid surface and the formation of a free surface vortex were investigated by various researchers such as Ryma *et al.* (2013), Motamedvaziri and Armenante (2012) and Patil *et al.* (2004). Moreover, higher magnitudes of axial velocity, turbulent kinetic energy and turbulent dissipation rate were obtained near to the free liquid surface, resulting in considerable entrainment of air into the liquid contained within the reactor vessel (Ryma *et al.* 2013; Deshmukh and Joshi 2006). Therefore, high clearance vessels are adopted for the surface aeration process in wastewater treatment plants (Patil *et al.* 2004). The flow patterns associated with standard, low and high clearance vessels are illustrated in Figs. 1(a)-1(c), respectively.

The transition from double-loop to single-loop down-pumping or up-pumping patterns has resulted

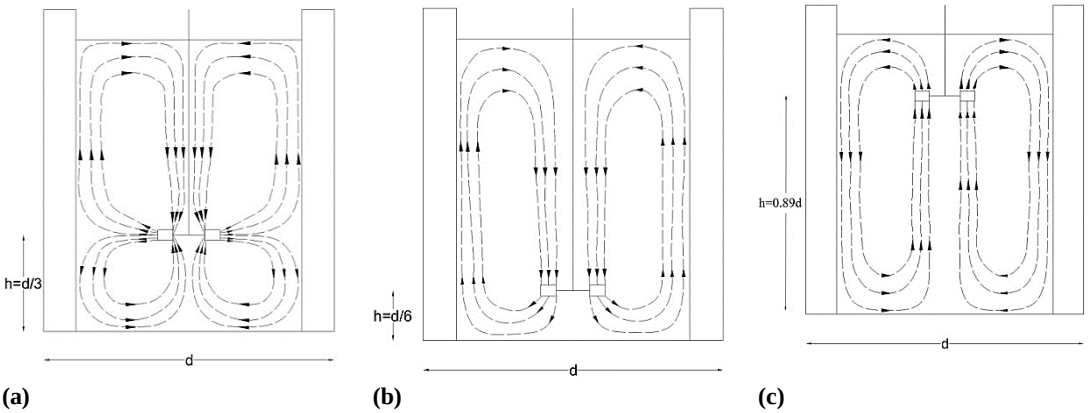

Fig. 1. Flow patterns associated with the (a) Standard configuration of the vessel, (b) Low clearance vessel and (c) High clearance vessel.

in a 25-30% reduction in the impeller power number (Ibrahim and Nienow 1995; Deshmukh and Joshi 2006) and a 16.37% decrease in the mixing time (Ochieng *et al*. 2008), respectively. The studies of Nienow (1968), Conti *et al*. (1981), Armenante *et al*. (1998), Armenante and Nagamine (1998), Montante *et al*. (1999, 2001a, 2001b), Galletti *et al*. (2003), Ochieng *et al*. (2008), Li *et al*. (2011) and Zhu *et al*. (2019) have determined a critical range of impeller clearance within which the double-loop to down-pumping single-loop flow pattern transition occurs. The flow pattern was found to be unstable within the critical range of impeller clearance and switched between double-loop and single-loop patterns with a well-defined periodicity (Zhu *et al*. 2019). Zhu *et al*. (2019) have described the necessary conditions for the development of a down-pumping single-loop pattern based on the impeller clearance and the distance between the impeller blades and the periphery of the reactor vessel. The critical impeller clearance for the transition from a double-loop to an up-pumping single-loop pattern was determined by Motamedvaziri and Armenante (2012) and Patil *et al*. (2019). The double-loop to down-pumping as well as up-pumping single-loop pattern transitions were unaffected by the rotational speed of the RT impeller (Li *et al*. 2011; Zhu *et al*. 2019; Motamedvaziri and Armenante 2012). On the other hand, smaller impellers at low clearance conditions easily produce a single-loop pattern compared to the larger impellers at low clearance conditions (Li *et al*. 2011; Zhu *et al*. 2019). Further, the down-pumping single-loop pattern produced by the RT impeller was found to be weaker than the single-loop pattern allied with the PBTD impeller (Zhu *et al*. 2019).

The CFD technique was effectively employed by Montante *et al*. (2001b), Deshmukh and Joshi (2006), Ochieng *et al*. (2008), Li *et al*. (2011), Motamedvaziri and Armenante (2012) and Zhu *et al*. (2019) for modeling the double-loop to down-pumping as well as up-pumping single-loop pattern transitions in agitated reactors. The CFD technique has provided detailed flow field characteristics related to the double-loop and single-loop down-pumping as well as up-pumping patterns in a faster manner compared to the experimental technique (Montante *et al*. 2001b). Moreover, the fluctuating quantities near the impeller can be efficiently modeled using the CFD technique, while the same can't be easily measured using the experimental techniques (Joshi *et al*. 2011). The Reynolds Averaged Navier–Stokes (RANS) approach was widely used by various scholars (Montante *et al*. 2001b; Zhu *et al*. 2019; Deshmukh and Joshi 2006) for modeling the double-loop to single-loop pattern transitions as accurate flow field results can be obtained at a relatively lower computational cost. Further, the various errors associated with the CFD modeling process need to be minimized and the respective predictions should be validated against the experimental results before drawing firm conclusions from the CFD models. Past studies have analyzed the characteristics of double-loop and single-loop down-pumping and up-pumping patterns, the critical range of impeller clearance within which the flow pattern transition occurs and the respective impacts on the power number of the impeller. However, the hydrodynamic reasons behind the transition from double-loop to single-loop down-pumping and up-pumping patterns and the decrease in the impeller power number during the double-loop to single-loop pattern transitions weren't discussed in the earlier studies. These aspects remain a mystery (Montante *et al*. 2001b; Zhu *et al*. 2019) and need to be evaluated to obtain clear relationships between the impeller clearance, flow field characteristics and various performance goals of the reactor vessel. The development of proper relationships between the impeller clearance, flow field characteristics and performance goals helps to select the optimal configuration of the reactor vessel for the underlying unit operations. Moreover, the variations in the characteristics of trailing vortices during the transition from double-loop to single-loop down-pumping and up-pumping patterns need to be evaluated as they significantly affect the mixing and mass transfer phenomena.

Thus, the objective of the present work is to develop CFD models of reactor vessels agitated using the RT impeller at various clearance levels in order to ascertain the physical aspects that cause the flow pattern transitions, the reduction in the impeller power number, the increase in the oxygen transfer and the variations in the characteristics of the trailing vortices.

2. REACTOR CONFIGURATIONS

A flat bottomed cylindrical tank with an inner diameter (d) and height (H) of 0.27m was used for modeling purposes. Four equally spaced baffle walls of width (B) 0.1d were extended throughout the entire height of the reactor vessel. An RT impeller with a diameter (D) of 0.093 m and six blades was concentrically mounted at various clearance levels (h/d) ranging from 0.11 to 0.89 so as to analyze the effect of the same in the underlying flow field conditions. The RT impeller was rotated at a speed (N) of 200 rpm in order to obtain the turbulent flow conditions (R_e = 29,000) in the tank. The RT impeller blade had a width (l) of D/4 and height (b) of D/5. Water at standard conditions was used as the working fluid for the modeling purposes. A summary of the reactor vessel configurations analyzed in the present study is given in Table 1. The sectional elevation and plan of the reactor vessel with the RT impeller at standard conditions is shown in Fig. 2.

3. COMPUTATIONAL METHODOLOGY

The three-dimensional steady state single-phase and transient multiphase CFD models were developed by simultaneously solving the continuity and momentum equations using the RANS approach. The Reynolds stresses obtained during the ensemble

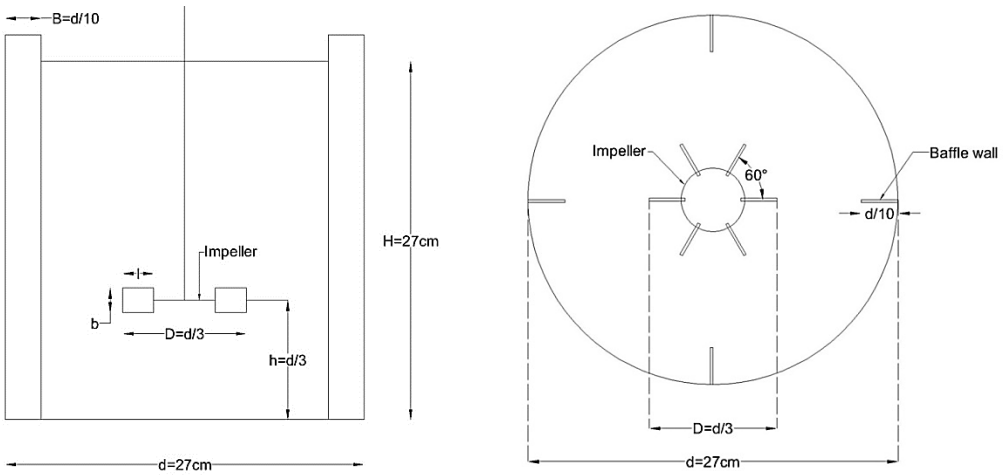

(a) **(b)**

Fig. 2. (a) Sectional elevation and (b) Plan of stirred tank reactor of standard configuration (Source: Wu and Patterson 1989).

Table 1. Summary of reactor vessel configurations

Reactor vessel parameter	Dimension (m)
d	0.27
H	0.27
B	0.027
D	0.093
h	0.03-0.24
N	200 rpm
l	0.023
b	0.019

averaging process were resolved using the standard *k-ε* turbulence model. Although various turbulence models such as Spalart-Allmaras, Shear Stress Transport, $k-w$ and Reynolds Stress Model were used for simulating the turbulent flows in the agitated reactors, the standard $k-\varepsilon$ model has provided accurate predictions (Alonzo-Garcia *et al.* 2019) for a wide range of flow problems at reasonable cost and thus was considered for the present work. The viscous flow of water close to the impeller and tank periphery was modeled using the standard wall function (Launder and Spalding 1974). The impeller-baffle interactions were simulated using the Multiple Reference Frame (MRF) technique. In the MRF technique, the reactor vessel was divided into two domains – the inner rotating zone and the outer stationary zone. The governing equations were solved in a rotating frame of reference in the inner zone and in a stationary frame of reference in the outer zone and the velocities from two frames of reference were suitably coupled at the interface separating the two domains. The entrainment of air into the reactor vessel was simulated using the implicit Volume of Fluid (VOF) method (Hirt and Nicholas 1981) with water and air as the working fluids. The effects of surface tension on the entrainment process were incorporated into the CFD model using the Continuum Surface Force (CSF) model and the coefficient of surface tension was fixed as 0.072 N/m, which is commonly adopted for the aeration process (Kulkarni and Patwardhan 2014). The time step adopted for the unsteady simulations was 0.0002s and the simulations were performed for a duration of 10s. The second order implicit time discretization was used for transient simulations. The impeller has made 35 revolutions when the simulations were stopped.

The low clearance vessels were modeled using the steady state single-phase approach since entrainment of air into the reactor vessel is negligible and only turbulent mixing of fluid within the vessel needs to be considered. The use of the transient multiphase modeling approach is not necessary for modeling the turbulent mixing as it will unnecessarily increase the computational cost of the modeling. On the other hand, standard and high clearance vessels provide sufficient entrainment of air into the reactor vessel; hence; the transient multiphase approach needs to be adopted for accurately modeling the respective phenomena.

The SIMPLE pressure-velocity coupling scheme was used to couple the ensemble averaged continuity and momentum equations and the resulting equations were numerically discretized using the second order upwind scheme. The performance of the second order upwind scheme was found to be highly comparable to that of the third order QUICK and the central differencing schemes (Coroneo *et al.* 2011; Deglon and Meyer 2006) and hence was adopted for the present work. During the multiphase conditions, the pressure term in the governing equations was discretized using the PRESTO scheme and the volume fraction term was discretized using the Geo-Reconstruct scheme. The RT impeller surfaces, baffle walls and tank periphery were modeled as solid boundaries with the no-slip boundary condition while the top surface of the tank was simulated using the symmetry boundary condition. During the multiphase modeling, the top surface of the tank was simulated using the pressure outlet condition. The power

number based on impeller torque (N_{pt}) and gas hold-up (e) were considered as the performance goals for the present study and the same are computed according to Eqs. (1) and (2), respectively, as given below. Also, the power number from the volume integrated turbulence dissipation rate ($N_{p\varepsilon}$) was computed to analyze the energy imbalance in the vessel as the energy given from the impeller should be dissipated in the tank periphery.

$$N_{pt} = P'/\{\rho N^3 D^5\} \quad (1)$$

Where $P' = 2\pi NT$, P' is the impeller power drawn, T is the net torque on the impeller blades and ρ is the density of fluid.

$$e = \{H_d\text{-}H\}/H_d \quad (2)$$

Where H_d and H are the height of the liquid in the presence as well as the absence of the gas.

The simulations were performed until the residuals of the continuity and momentum equations were reduced below 10^{-7} and the monitoring parameters such as impeller power number and volume integrated turbulence dissipation rate reached a constant magnitude. The simulations were performed in a workstation with a double precision 64 bit Intel (R) Xeon (R) E5-1620 3.6 GHz processor with 12 cores. The details of the standard k-ε model, the VOF method, the MRF impeller modeling scheme, the pressure-velocity coupling schemes and the numerical discretization schemes are elucidated in ANSYS (2013).

The CFD models of the reactor vessels were developed using commercially available ANSYS FLUENT software (version 17.0). The three-dimensional geometry of the reactor vessels was generated and spatially discretized using the ANSYS meshing tool. The hybrid grid consisting of tetrahedral elements in the inner zone and hexahedral elements in the outer zone was used for modeling the reactor flow fields. The hybrid grid developed for the standard configuration of the vessel is shown in Fig. 3. The thicknesses of the impeller and baffle walls were properly included by providing suitable local refinements and the inflation layers were adopted around the impeller for resolving the boundary layer gradients. The grid independence study was performed by successively reducing the size of tetrahedral elements comprising the RT impeller. The details of the grids generated for the grid independence study are given in Table 2.

Table 2. Details of the grids used for grid independence study

Grid	Impeller element size (m)	Number of elements	Number of nodes
Grid 1	0.004000	300573	304574
Grid 2	0.000800	996072	361096
Grid 3	0.000350	4497937	1325522
Grid 4	0.000258	7418360	2329381
Grid 5	0.000240	8451837	2607928

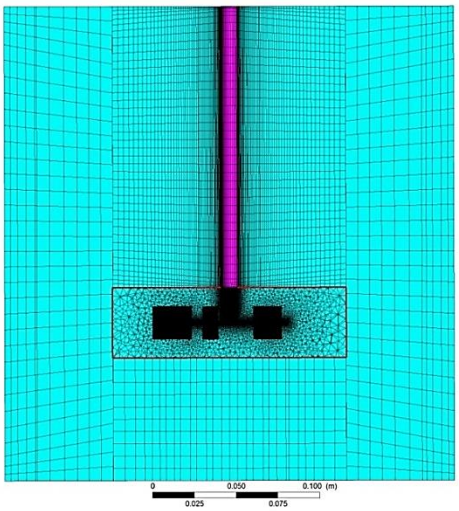

Fig. 3. Hybrid grid developed for the reactor vessel (longitudinal section).

The computational methodology adopted for the numerical simulations needs to be verified and validated so as to provide reliable and accurate predictions of the various flow field quantities. The standard configuration of the reactor vessel was considered for this process as the underlying mean velocity and turbulent flow fields were widely investigated in the past using advanced experimental and computational methods (Wu and Patterson 1989; Lee and Yianneskis 1998; Delafosse *et al*. 2008; Zhang *et al*. 2017). The variations of flow parameters such as N_{pt}, $N_{p\varepsilon}$ and the axial profile of normalized mean radial velocity (u_r/u_{tip}) close to the impeller with the grid resolution are shown in Figs. 4(a)-4(b). $N_{p\varepsilon}$ is computed by integrating the turbulence dissipation rate in the entire volume of the vessel and normalizing by a factor of N^3D^5. The equation for $N_{p\varepsilon}$ is given in Eq. (3).

$$N_{p\varepsilon} = \frac{\iiint \rho\varepsilon \, dV}{\rho N^3 D^5} \quad (3)$$

As illustrated in Figs. 4(a) and 4(b), N_{pt} and normalized mean radial velocity increase from Grid 1 to Grid 2 and remain constant thereafter. On the other hand, $N_{p\varepsilon}$ increases from Grid 1 to Grid 4 and provides negligible variations with Grid 5. The numerical convergence of the mean and turbulent flow quantities were analyzed using the Grid Convergence Index (GCI) (Roache 1994) concept. The GCI of N_{pt}, $N_{p\varepsilon}$ and the peak mean radial velocity computed from Grid 4 were less than 5%. This indicates superior convergence of N_{pt}, $N_{p\varepsilon}$ and peak mean radial velocity with Grid 4. Therefore, the flow field results from Grid 4 are independent of the grid resolution and can be used for validation purposes. The grid independence study was performed in a similar manner for the remaining reactor configurations considered for the analysis.

In the validation process, the predictions of N_{pt}, $N_{p\varepsilon}$ and mean radial velocity from the optimal grid (Grid 4) were compared with the corresponding experimental results of Bates *et al*. (1963) and Wu and Patterson (1989). The experimental results

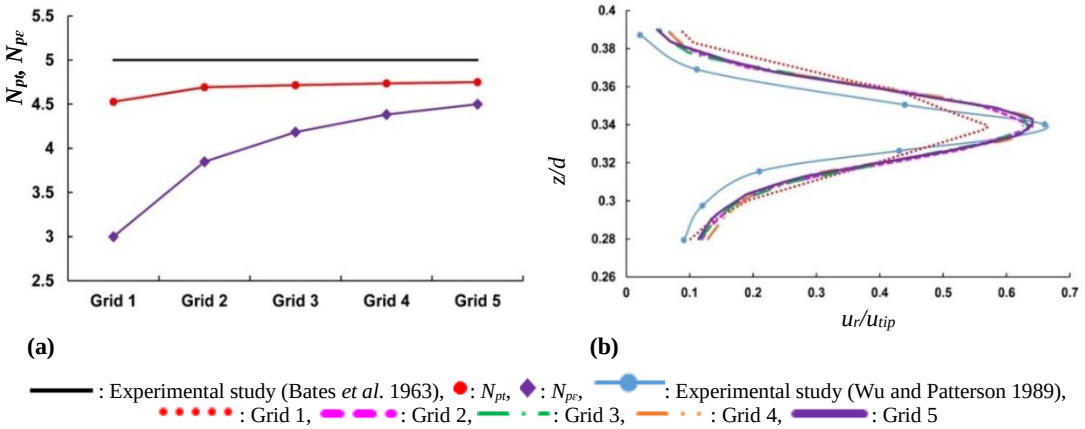

Fig. 4. Variations of (a) N_{pt}, $N_{p\varepsilon}$ and (b) axial profile of u_r/u_{tip} close to the impeller with grid resolution.

represent the real or benchmark values of the flow field characteristics which can be compared with the numerical predictions to analyze the accuracy of the CFD models. N_{pt} and $N_{p\varepsilon}$ were accurately predicted with errors of less than 5% and 10%, respectively. The axial profile of the normalized radial velocity obtained from Grid 4 was close to the corresponding experimental profile and the magnitude and location of peak radial velocity were accurately predicted. The energy imbalance $\{[N_{pt}-N_{p\varepsilon}]/N_{pt}\}$ associated with the reactor vessel was reduced to 10%, while higher values (more than 20%) can be observed in the review article of Joshi *et al*. (2011). The variation of N_{pt} with the impeller clearance is shown in Fig. 5. Abrupt reduction of N_{pt} with a decrease in the impeller clearance was found between the *h*/*d* of 0.15 and 0.22, which is in line with the observations of Montante *et al*. (1999, 2001b).

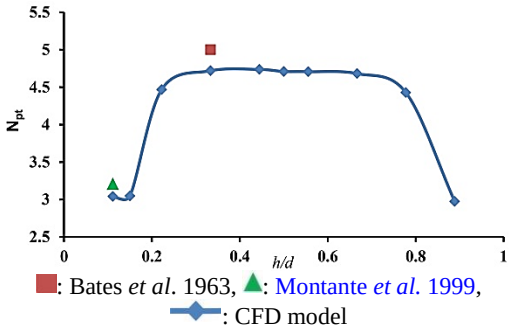

Fig. 5. Variation of N_{pt} with *h*/*d*.

Also, the N_{pt} related to the configuration with *h*/*d* of 0.15 was accurately predicted by the present CFD model with a relative deviation of 5%. The radial profile of axial velocity at 3 cm below the impeller surface obtained from the LDA measurements of Montante *et al*. (2001b) for the low clearance configuration with *h*/*d* of 0.15 was compared with the CFD predictions from the present study, as illustrated in Fig. 6.

The present CFD model accurately predicts the axial velocity magnitudes along the entire radial profile considered for the analysis. The magnitudes and locations of maximum and minimum axial velocity were also accurately predicted, indicating the proper replication of the down-pumping discharge stream emerging from the impeller. Thus, the present CFD modeling approach accurately predicts the mean and turbulent flow field characteristics associated with the various reactor configurations and can be confidently employed for further analysis and interpretations.

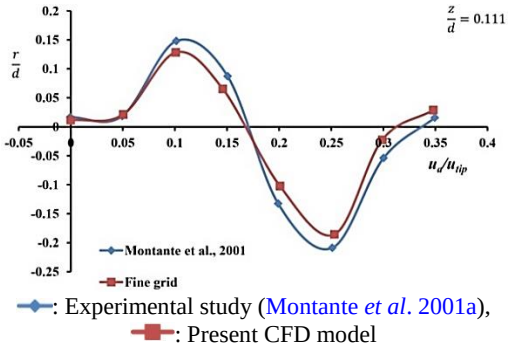

Fig. 6. Radial profile of axial velocity at 3 cm below the impeller surface for *h*/*d* of 0.15.

4. RESULTS AND DISCUSSION

The mean and turbulent flow field characteristics associated with the reactor vessels agitated using the RT impeller at various clearance levels are analyzed in this section. Hydrodynamic factors causing the variations in the flow patterns, impeller power number and oxygen transfer characteristics with the variations in the RT impeller clearance are elucidated from this analysis.

4.1. Impeller Power Number

The variation of N_{pt} with the impeller clearance is shown in Fig. 5. The *h*/*d* between 0.4 and 0.6 provide similar values of N_{pt} and are specified as the medium range of impeller clearance hereafter. On the other hand, *h*/*d* less than 0.4 and more than 0.6 develop N_{pt} values which are 35% lower

compared to the medium range of impeller clearance and are recognized as lower and higher ranges of impeller clearance, respectively. The reduction of N_{pt} at the h/d of 0.10 obtained from this study is close to that reported by Montante *et al.* (1999 and 2001). Also, the lower and higher ranges of impeller clearance generate similar predictions of N_{pt}. Therefore, for the further hydrodynamic analysis, the flow field results from three reactor configurations, namely, standard vessel (h/d = 0.33), low clearance vessel (h/d = 0.167) and high clearance vessel (h/d = 0.89), are considered. These configurations are specified as Std-C, Low-C and High-C, respectively, hereafter in this manuscript.

4.2. Oxygen Transfer Characteristics

The oxygen transfer characteristics associated with the higher range of impeller clearance were studied in detail as the medium and lower ranges of impeller clearance provide poor entrainment of air. However, the oxygen transfer characteristics of Std-C were also considered in order to ascertain the increase in the entrainment levels with the increase in the impeller clearance. Therefore, the reactor vessels with the RT impeller at clearance levels of 0.33*d*, 0.78*d* and 0.89*d* were considered for analyzing the oxygen transfer characteristics. The variation of gas hold-up with the RT impeller clearance level is shown in Fig. 7. From Fig. 7, it is clear that the gas hold-up increases with an increase in impeller clearance and attains maximum magnitude for the reactor vessel with a clearance level of 0.89*d*. This observation is in line with the inference of Patil *et al.* (2004) that the oxygen transfer into the reactor vessel attains peak magnitude when the RT impeller is located close to the free liquid surface.

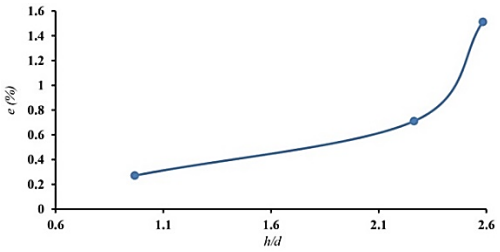

Fig. 7. Variation of gas hold-up with *h/d*.

4.3. Mean and Turbulent Flow Characteristics

The variations of pressure, trailing vortex structures, turbulent kinetic energy, flow patterns, volume fraction of air, vorticity and strain rate with the impeller clearance are shown in Figs. 8-17. The distribution of pressure (P) is evaluated in terms of pressure coefficient (C_p), as mentioned in Eq. (4) and the same obtained for Low-C, Std-C and High-C are illustrated in Figs. 8(a)-8(c).

$$C_p = P/\{0.5\rho \boldsymbol{u}_{tip}^2\} \quad (4)$$

The trailing vortices are plotted based on the Q-criterion (Huang and Green 2015) which is specified as given in Eq. (5).

$$Q = 0.5\{[w^2 - s^2]\} > 0 \quad (5)$$

where w is the Euclidean norm of rotation rate tensor and s indicates the Euclidean norm of strain rate tensor. The formation of a vortex is inferred when $Q > 0$, i.e., the rotation rate of a fluid element dominates over the respective strain rate.

As shown in Fig. 8(b), Std-C develops higher magnitudes of pressure near the impeller surface and uniform distribution of pressure in the entire domain of the reactor vessel. Low-C generates a distinct region of low pressure near the bottom surface of the reactor vessel, as shown in Fig. 8(a), whereas High-C produces a distinct region of low pressure near the top surface of the tank, as indicated in Fig. 8(c). The blade on the right side of the shaft indicates the suction side or back side, while that on the left side indicates the pressure side or front side. Std-C provides a higher pressure difference between the suction and pressure sides of the blades, while Low-C and High-C develop a lower pressure difference between the suction and pressure sides of the blades.

As displayed in Figs. 11(a)-11(c), Std-C develops stronger discharge streams from the impeller which move radially and strike on the tank periphery to generate a double re-circulation pattern. On the other hand, Low-C generates discharge streams which are inclined toward the bottom surface of the reactor vessel and provides a single-loop down-pumping pattern. Moreover, secondary flow the reactor vessel.

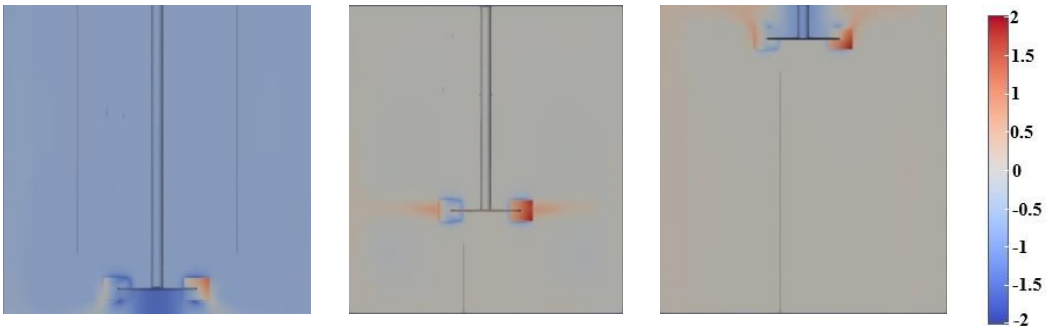

(a) **(b)** **(c)**

Fig. 8. Contours of pressure coefficient for (a) Low-C, (b) Std-C and (c) High-C along the mid-baffle plane

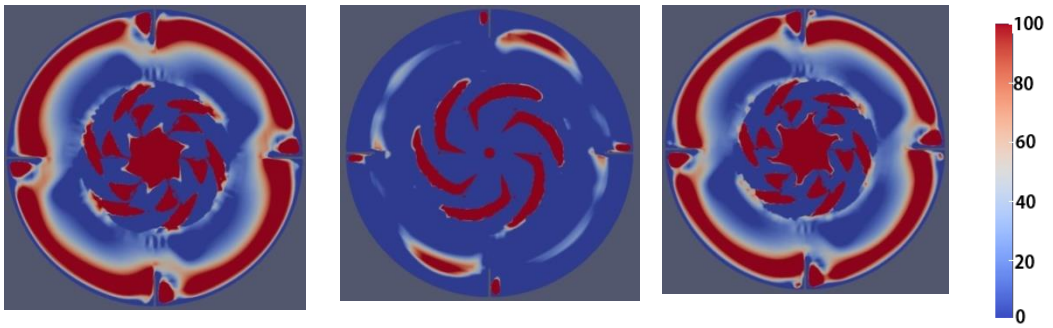

(a) (b) (c)

Fig. 9. Contours of trailing vortices along impeller center plane for (a) Low-C, (b) Std-C and (c) High-C.

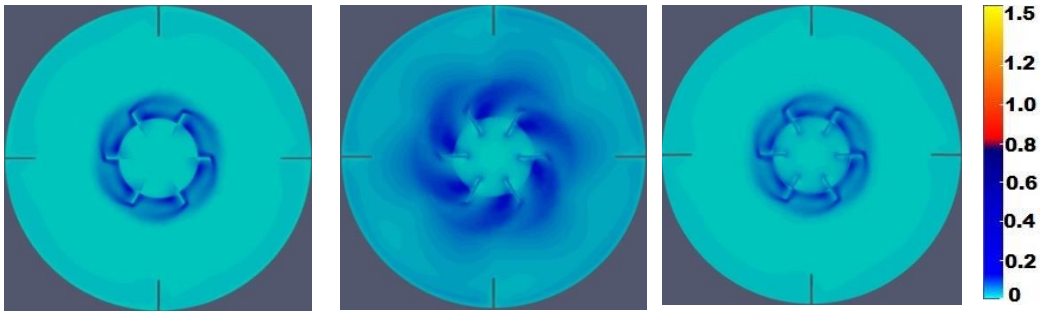

(a) (b) (c)

Fig. 10. Contours of turbulent kinetic energy along the impeller center plane for (a) Low-C, (b) Std-C and (c) High-C.

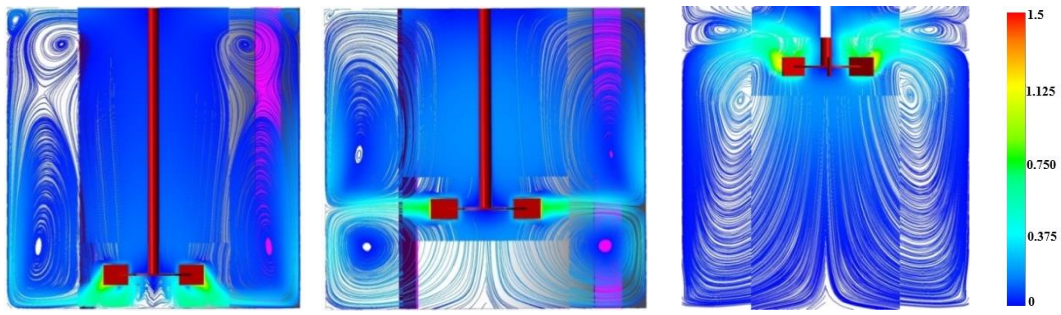

(a) (b) (c)

Fig. 11. Flow patterns associated with (a) Low-C, (b) Std-C and (c) High-C along the mid-baffle plane.

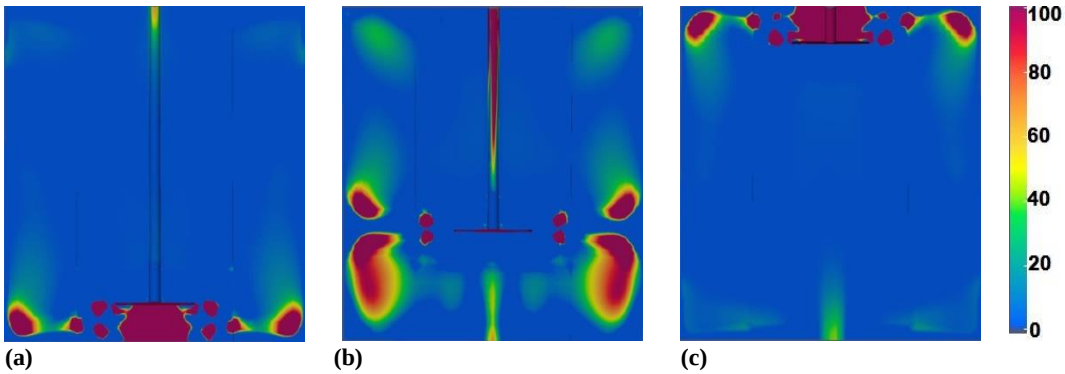

(a) (b) (c)

Fig. 12. Contours of trailing vortices along the mid-baffle plane for (a) Low-C, (b) Std-C and (c) High-C.

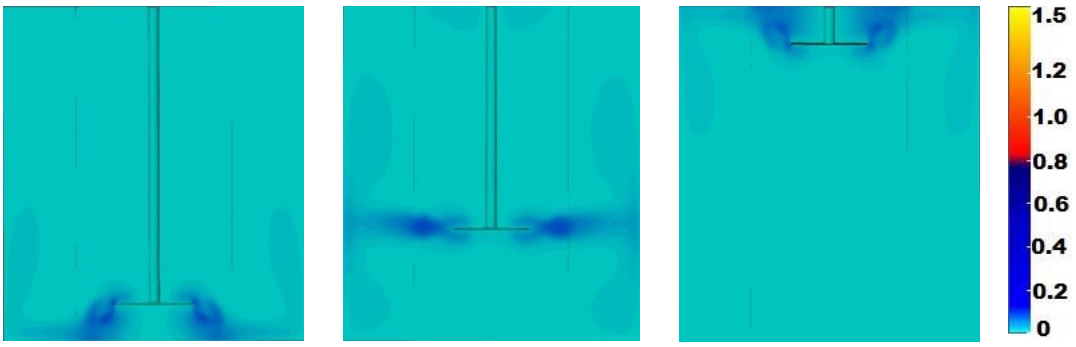

(a) (b) (c)

Fig. 13. Contours of turbulent kinetic energy along the mid-baffle plane for (a) Low-C, (b) Std-C and (c) High-C.

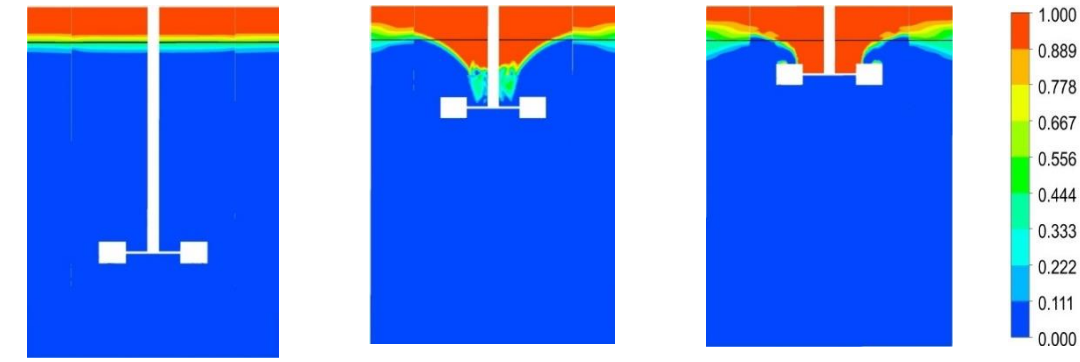

(a) (b) (c)

Fig. 14. Contours of volume fraction of air at *h*/*d* of (a) 0.33, (b) 0.78 and (c) 0.89 (Black line in the Figs. indicates air-water interface before the commencement of simulations).

structures such as smaller circulation loops can be seen below the right corners of the blades and the top surface of the reactor vessel. High-C produces discharge streams which are inclined toward the top surface of the reactor vessel and develop a single-loop up-pumping pattern. Also, several smaller circulation loops can be seen near the top surface of

According to Figs. 9(a)-9(c), Std-C provides larger trailing vortex structures which extend to a larger radial distance behind the impeller blades. On the other hand, Low-C and High-C develop smaller trailing vortex structures which extend to a smaller radial distance behind the impeller blades. The movement of the impeller blades of Std-C generates a pair of counter-rotating coherent trailing vortices above and below the impeller center plane on the rear sides of the blades which follow the trajectory of the discharge streams emerging from the impeller (Fig. 12(b)). Compared to the standard reactor vessel, Low-C provides only a pair of trailing vortices below the impeller center plane which follow the trajectory of down-pumping discharge streams emerging from the impeller (Fig. 12(a)). High-C develops a pair of trailing vortices above the impeller center plane which follow the trajectory of up-pumping discharge streams emerging from the impeller (Fig. 12(c)).

The variation of the volume fraction of air with the impeller clearance is shown in Figs. 14(a)-14(c). Based on the contours of the volume fraction air, it can be inferred that the clearance level of 0.33*d* provides an undisturbed air-water interface resulting in negligible entrainment of air into the reactor vessel. On the other hand, the higher clearance levels of 0.78*d* and 0.89*d* exhibit substantial deflection and deformation of the free liquid surface, leading to the formation of a free surface vortex. The free surface vortex touches the impeller surface at the clearance level of 0.89*d*, resulting in the flooding of air bubbles and a substantial increase of more than 53% in the magnitude of gas hold-up compared to the reactor vessel with a clearance level of 0.78*d*.

Figures 10, 13, 17, 15 and 16 represent contours of normalized turbulent kinetic energy along the impeller center plane and mid-baffle plane, contours of vorticity and the strain rate for various clearance levels. The distribution of turbulent kinetic energy follows the corresponding trajectory of discharge streams and trailing vortex structures. Std-C produces higher turbulent kinetic energy near the impeller which reduces toward the periphery of the reactor vessel (Fig. 13(b)). Low-C provides higher turbulent kinetic energy below the impeller which extends to the bottom surface of the reactor vessel (Fig. 13(a)). On the other hand, High-C develops higher turbulent kinetic energy above the impeller which progresses to the top surface of the reactor vessel (Fig. 13(c)). Further, a considerable increase in the magnitudes of vorticity, strain rate and

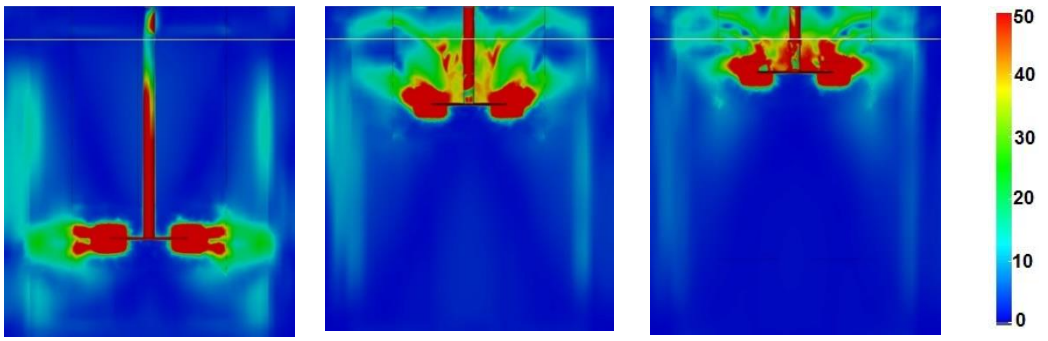

(a) (b) (c)

Fig. 15. Contours of vorticity at *h*/*d* of (a) 0.33, (b) 0.78 and (c) 0.89 (White line in the Figs. indicates air-water interface before the commencement of simulations).

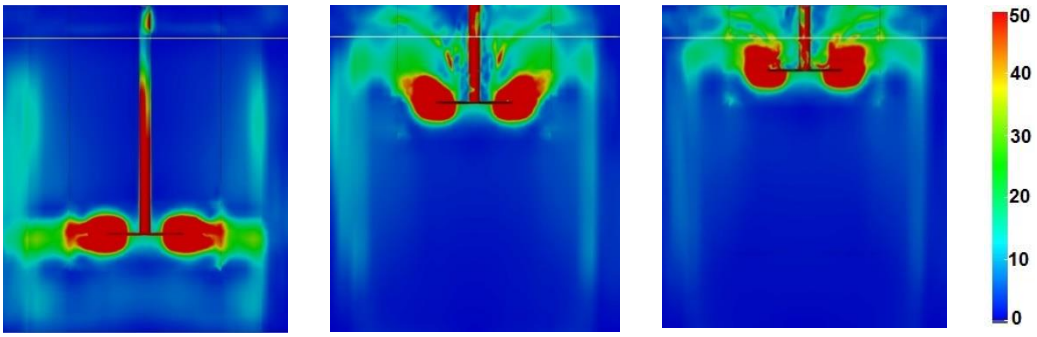

(a) (b) (c)

Fig. 16. Contours of strain rate at *h*/*d* of (a) 0.33, (b) 0.78 and (c) 0.89 (White line in the Figs. indicates air-water interface before the commencement of simulations).

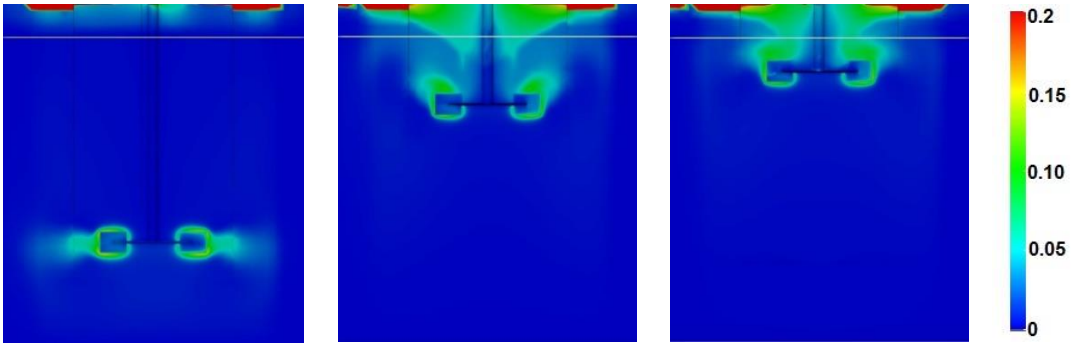

(a) (b) (c)

Fig. 17. Contours of turbulent kinetic energy at *h*/*d* of (a) 0.33, (b) 0.78 and (c) 0.89 (White line in the Figs. indicates air-water interface before the commencement of simulations).

turbulent kinetic energy on the air side of the interface was noted for the higher clearance levels of 0.78*d* and 0.89*d*, respectively, in comparison with Std-C (Figs. 15-17). Therefore, an increase or decrease in the impeller clearance causes changes in the distribution of pressure, flow patterns, vortex and turbulent flow characteristics.

4.4. Physical Reasons for Variations in the Performance Characteristics

This sub-section attempts to relate the mean and turbulent flow field characteristics from various reactor configurations with the corresponding performance goals.

The distribution of pressure on the suction and pressure sides of the blades controls the impeller torque and thus the N_{pt} magnitudes. The higher pressure difference between the suction and pressure sides of the blades of Std-C leads to higher torque and N_{pt} related to the rotating impeller, whereas the lower pressure difference between the suction and pressure sides of the blades of Low-C and High-C provides lower torque and N_{pt} related to the rotating impeller. The pressure distribution on the suction sides of the blades is controlled by the low pressure regions developed behind the blades due to strong rotation of the impeller. These low pressure regions separate from the blades and move toward the periphery of the vessel and are termed

flow separation regions. These flow separation regions are characterized by trailing vortex structures. The larger and longer trailing vortices related to Std-C develop stronger flow separation regions behind the impeller blades which substantially decreases the pressure on the suction sides of the blades, leading to higher form drag and torque associated with the rotating impeller. On the other hand, smaller and shorter trailing vortices allied with the Low-C and High-C generate weaker flow separation regions behind the impeller blades which significantly increase the pressure on the suction sides of the blades, leading to lower form drag and torque of the rotating impeller. The increase or decrease in the torque of the impeller leads to the corresponding increase or decrease in the impeller power number. Moreover, Std-C produces a greater extent of high turbulent kinetic energy behind the impeller blades, as shown in Fig. 10(b), while Low-C and High-C provide a lesser extent of high turbulent kinetic energy behind the blades, as illustrated in Figs. 10(a) and 10(c), respectively. The increase or decrease in N_{pt} with variations in the impeller clearance can be correlated to the corresponding variations in the intensity and extent of turbulent kinetic energy behind the impeller blades. Thus, the strength and distributions of pressure, trailing vortices and turbulent kinetic energy behind the impeller blades control the torque and N_{pt} related to the reactor vessels.

The uniform pressure distribution associated with Std-C produces discharge streams which radially move toward the periphery of the reactor and develop a double re-circulation pattern. The low pressure region generated below the impeller of Low-C drags the discharge streams toward the bottom surface of the vessel. The downward discharge streams strike on the bottom surface of the vessel and then move upward, resulting in the formation of a down-pumping single re-circulation pattern. In a similar manner, the low pressure region developed above the impeller of High-C deflects the discharge streams upward toward the top surface of the reactor vessel. These upward discharge streams strike on the free liquid surface and move downward, leading to the formation of an up-pumping single re-circulation pattern. Hence, the distribution of pressure near the impeller controls the flow pattern produced within the reactor vessel. The double-loop and single-loop down-pumping patterns obtained from this study are similar to that reported by Montante *et al.* (1999, 2001b).

The double- to single-loop down-pumping and up-pumping flow pattern transitions affect the characteristics of trailing vortices associated with these reactor configurations. Std-C develops larger trailing vortex structures behind the impeller blades. On the other hand, shifting the RT impeller to near the bottom or top surfaces of the reactor vessel results in smaller trailing vortex structures behind the blades and multiple smaller vortices around the impeller. In other words, the larger trailing vortex structures associated with Std-C are transformed into smaller trailing vortices and several smaller vortex structures around the RT impeller as the impeller is shifted toward the bottom or top surfaces of the reactor vessel. This kind of variation in the energy cascade or energy transfer with the variations in the impeller clearance was also observed by Galletti and Brunazzi (2011). The secondary flow features related to Low-C and High-C may also have a vital role in the characteristics of corresponding vortex structures. The upward discharge streams associated with High-C facilitate the formation of a free surface vortex near the impeller. The free surface vortex thus formed increases the entrainment of air into the reactor vessel as the interfacial area of the same is many times greater than the flat air-water interface. The single-loop pattern developed in the reactor vessel carries the entrained air into the bulk volume of the liquid contained in the tank. Moreover, the strong shearing action of the RT impeller breaks the free surface vortex and increases the ingestion of air bubbles into the liquid contained within the reactor vessel. The multiple vortices developed near the free liquid surface, as illustrated in Fig. 12(c), increase the localized mixing near the free liquid surface and in turn improve the oxygen transfer into the reactor vessel.

Further, a considerable increase in the magnitudes of vorticity, strain rate and turbulent kinetic energy on the air side of the interface associated with the higher clearance levels of 0.78d and 0.89d as illustrated in Figs. 15-17 can be correlated to the corresponding increase in the entrainment of air. Thus, the low pressure region developed near the free liquid surface and higher vortex and turbulent activity on the air side of the interface control the surface aeration process in the reactor vessels.

The mixing characteristics associated with Std-C, Low-C and High-C were analyzed using the profiles of turbulent dissipation rate and turbulence intensity. The volume averaged turbulence dissipation rate related to these vessel configurations is illustrated in Fig. 18. The axial profiles of normalized turbulence intensity and the turbulence dissipation rate near the impeller along the mid-baffle plane for these reactor vessels are shown in Figs. 19 and 20, respectively. The overall turbulence dissipation rate associated with Std-C is 35% more than that of Low-C and High-C. The axial profiles of turbulence parameters elucidate the nature of mixing conditions present in the reactor vessel. The peak turbulent dissipation rate and turbulence intensity from Std-C are higher than that of Low-C and High-C. The higher turbulent activity in the middle portion of Std-C generates bulk mixing of fluid within the reactor vessel. On the other hand, Low-C provides superior turbulence action near the bottom surface of the reactor vessel. This in turn provides localized mixing conditions which are suitable for lifting the solids and subsequent suspension of the same (Mollaabbasi and Najmabad, 2016) in the liquid contained within the reactor vessel. Similarly, High-C generates superior turbulence action near the free liquid surface of the reactor vessel. This eventually generates localized mixing near the free liquid

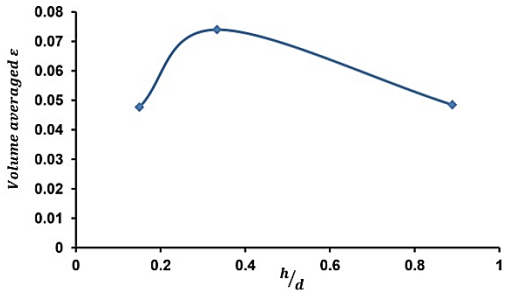

Fig. 18. Variation of volume averaged ε with *h/d*.

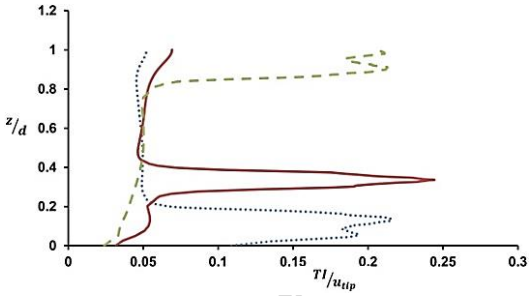

Fig. 19. Variation of TI/u_{tip} with *h/d*.

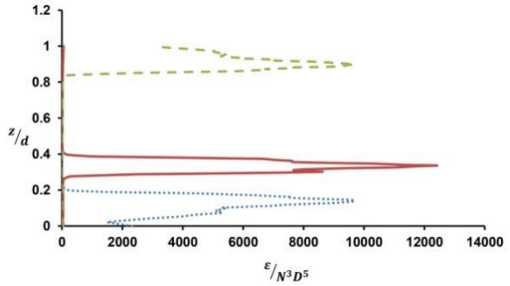

Fig. 20. Variation of ε/N^3D^5 with *h/d*

surface which results in the formation of a free surface vortex and subsequent entrainment of air into the reactor vessel. Therefore, the nature of the mixing process varies with the impeller clearance and controls the performance of the agitated reactor vessels.

In short, the development of a low pressure region above or below the impeller causes a transition from a double-loop to a single-loop pattern and varies the corresponding vortex and turbulence characteristics. The variations in the vortex and turbulence characteristics in turn affect the mixing performance of the reactor vessel.

5. CONCLUSIONS

The CFD simulations of a baffled reactor vessel agitated using the RT impeller at various clearance levels were performed to explain the variations in the flow patterns, power number and oxygen transfer rates. The standard *k-ε* model coupled with the MRF impeller modeling scheme provided reliable and accurate predictions of the underlying mean and turbulent flow fields.

The classic double-loop pattern associated with the standard reactor vessel changed into a single-loop down-pumping pattern under lower clearance conditions and a single-loop up-pumping pattern under higher clearance conditions. The formation of a distinct low pressure region near the bottom surface of the low clearance vessel and the top surface of the high clearance vessel led to the development of a down-pumping single-loop pattern and an up-pumping single-loop pattern. The down-pumping discharge streams increased the vortex and turbulence characteristics near the bottom surface of the low clearance vessels, while the up-pumping discharge streams increased the same near the top surface of the high clearance vessels. The larger and longer trailing vortices associated with the standard reactor vessel were transformed into smaller trailing vortices and multiple vortex structures surrounding the impeller under low and high impeller clearances, respectively. The reduction in the size and length of the trailing vortices behind the impeller blades of low and high clearance vessels resulted in the formation of weak flow separation regions and a subsequent decrease in the form drag and torque of the rotating impeller. This explains the decrease in N_{pt} in Low-C and High-C compared to Std-C.

The high clearance vessels provided higher oxygen transfer compared to the standard reactor vessel and the maximum gas hold-up was obtained for the reactor vessel with the RT impeller located near the free liquid surface. The development of a free surface vortex due to the upward discharge streams and subsequent shearing action of the impeller increased the entrainment of air into the liquid. Moreover, significant vortex and turbulence activity on the air side of the air-water interface was obtained for the high clearance vessels compared to the standard reactor vessel, elucidating the respective impact on the surface aeration process. The free surface vortex associated with the reactor vessel with a clearance level of 0.89*d* touched the impeller surface, leading to the flooding of air bubbles and a considerable increase in the gas hold-up magnitude. The standard reactor vessel produced superior bulk mixing conditions, whereas the low and high clearance vessels generated localized mixing conditions near the bottom and top surfaces of the reactor vessels, respectively. The overall turbulence dissipation rate related to the standard reactor vessel was 35% more than that of the low and high clearance vessels. Thus, the distributions of pressure, trailing vortex and turbulence characteristics in the reactor agitated using the RT impeller vary with the impeller clearance and control the underlying flow patterns, power number and oxygen transfer processes.

ACKNOWLEDGEMENTS

This work was supported by the Science and Engineering Research Board (SERB) under Grant [grant SB/S3/CEE/0057/2013], Government of India.

REFERENCES

Alonzo-Garcia, A., V. X. Mendoza-Escamilla, S. A. Martinez-Delgadillo, I. Gonzalez-Neria, C. C. Gutiérrez-Torres and J. A. Jiménez-Bernal (2019). On the Performance of Different RANS Based Models to Describe the Turbulent Flow in an Agitated Vessel using Non-Structured Grids and PIV Validation. *Brazilian Journal of Chemical Engineering* 36(1), 361-382.

ANSYS (2013). *ANSYS Fluent Theory Guide*. ANSYS, Inc., Canonsburg, USA.

Armenante, P. M., E. U. Nagamine and J. Susanto (1998). Determination of Correlations to Predict the Minimum Agitation Speed for Complete Solid Suspension in Agitated Vessels. *Canadian Journal of Chemical Engineering* 76(3), 413–419.

Armenante, P. M. and E. U. Nagamine (1998). Effect of low off-bottom impeller clearance on the minimum agitation speed for complete suspension of solids in stirred tanks. *Chemical Engineering Science* 53(9), 1757–1775.

Bates, R. L., P. L. Fondy and R. R. Corpstein (1963). An Examination of Some Geometric Parameters of Impeller Power. *I & EC Process Design & Development* 2(4), 310–314.

Conti, R., S. Sicardi and V. Specchia (1981). Effect of the stirrer clearance on particle suspension in agitated vessels. *Chemical Engineering Journal* 22(3), 247–249.

Coroneo, M., G. Montante, A. Paglianti and F. Magelli (2011). CFD prediction of fluid flow and mixing in stirred tanks: Numerical issues about the RANS simulations. *Computers & Chemical Engineering* 35, 1959-1968.

Debab, A., N. Chergui, K. Bekrentchir and J. Bertrand (2011). An Investigation of Heat Transfer in a Mechanically Agitated Vessel. *Journal of Applied Fluid Mechanics* 4(2), 43-50.

Deglon, D. A. and C. J. Meyer (2006). CFD modelling of stirred tanks: Numerical considerations. *Minerals Engineering* 19, 1059-1068.

Delafosse, A., A. Line, J. Morchain and P. Guiraud (2008). LES and URANS simulations of hydrodynamics in mixing tank: Comparison to PIV experiments. *Chemical Engineering Research & Design* 86, 1322-1330.

Deshmukh, N. A. and J. B. Joshi (2006). SURFACE AERATORS: Power Number, Mass Transfer Coefficient, Gas Hold up Profiles and Flow Patterns. *Chemical Engineering Research and Design* 84(A11), 977-992.

Escudie, R., D. Bouyer and A. Line (2004). Characterization of Trailing Vortices Generated by a Rushton Turbine. *AIChE Journal* 50(1), 75-86.

Escudie, R. and A. Line (2003). Experimental Analysis of Hydrodynamics in a Radially Agitated Tank. *AIChE Journal* 49(3), 585-603.

Galletti, C. and E. Brunazzi (2011). *Flow Instabilities in Mechanically Agitated Stirred Vessels.* In Tech, Rijeka, Croatia.

Galletti, C., E. Brunazzi, M. Yianneskis and A. Paglianti (2003). Spectral and wavelet analysis of the flow pattern transition with impeller clearance variations in a stirred vessel. *Chemical Engineering Science* 58(17), 3859–3875.

Hirt, C. W. and B. D. Nicholas (1981). Volume of fluid method for the dynamics of free surface boundaries. *Journal of Computational Physics* 39, 201-225.

Huang, Y. and M. A. Green (2015). Detection and tracking of vortex phenomena using Lagrangian coherent structures. *Experiments in Fluids* 56(147), 1-12.

Ibrahim, S. and A. W. Nienow (1995). Power curves and flow patterns for a range of impellers in Newtonian fluids: $40<Re<5\times10^5$. *Trans IChemE* 73 Part A(5), 485–491.

Joshi, J. B., N. K. Nere, C. V. Rane, B. N. Murthy, C. S. Mathpati, A. W. Patwardhan and V. V. Ranade (2011). CFD simulation of stirred tanks: Comparison of turbulence models. Part I: Radial flow impellers. *Canadian Journal of Chemical Engineering* 89, 23–82.

Karpinska, A. M. and J. Bridgeman (2016). CFD-aided modelling of activated sludge systems- A critical review. *Water Research* 88, 861-879.

Kulkarni, A. L. and A. W. Patwardhan (2014). CFD modeling of gas entrainment in stirred tank systems. *Chemical Engineering Research & Design* 92, 1227-1248.

Launder, B. E. and D. B. Spalding (1974). The Numerical Computation of Turbulent Flows. *Computer Methods in Applied Mechanics & Engineering* 3, 269–289.

Lee, K. C. and M. Yianneskis (1998). Turbulence properties of the impeller stream of a rushton turbine. *AIChE Journal* 44(1), 13-24.

Li, L. C., N. Chen, K. F. Xiang and B. P. Xiang (2020). A Comparative CFD Study on Laminar and Turbulent Flow Fields in Dual-Rushton Turbine Stirred Vessels. *JAFM* 13(2), 413-427.

Li, Z., Y. Bao and Z. Gao (2011). PIV experiments and large eddy simulations of single-loop flow fields in Rushton turbine stirred tanks. *Chemical Engineering Science* 66(6), 1219–1231.

Mollaabbasi, R. and J. M. Najmabad (2016). Experimental Investigation and Optimization of Solid Suspension in Non-Newtonian Liquids at High Solid Concentration. *JAFM* 9(4), 1907-1914.

Montante, G., K. C. Lee, A. Brucato and M. Yianneskis (2001a). Experiments and predictions of the transition of the flow pattern with impeller clearance in stirred tanks. *Computers & Chemical Engineering* 25(4), 729–735.

Montante, G., K. C. Lee, A. Brucato and M. Yianneskis (2001b). Numerical simulations of the dependency of flow pattern on impeller clearance in stirred vessels. *Chemical Engineering Science* 56(12), 3751–3770.

Montante, G., K. C. Lee, A. Brucato and M. Yianneskis (1999). An Experimental Study of Double-to Single-Loop Transition in Stirred Vessels. *Canadian Journal of Chemical Engineering* 77(4), 649–659.

Motamedvaziri, S. and P. M. Armenante (2012). Flow regimes and surface air entrainment in partially filled stirred vessels for different fill rations. *Chemical Engineering Science* 81, 231-250.

Nienow, A. W. (1968). Suspension of solid particles in turbine agitated baffled vessels. *Chemical Engineering Science* 23(12), 1453–1459.

Ochieng, A., M. S. Onyango, A. Kumar, K. Kiriamiti and P. Musonge (2008). Mixing in a tank stirred by a Rushton turbine at a low clearance. *Chemical Engineering Processing* 47(5), 842–851.

Patil, H., A. K. Patel, K. Devarajan and A. Venu Vinod (2019, December). Comparison of Different off Bottom Impeller Clearances to Investigate the Effect on Hydrodynamics in Rushton Turbine Stirred Tank. In *Proceedings of the International Conference on New Frontiers in Chemical, Energy and Environmental Engineering (INCEEE-2019)*, NIT Warangal, Telangana, India.

Patil, S. S., N. A. Deshmukh and J. B. Joshi (2004). Mass-Transfer Characteristics of Surface Aerators and Gas-Inducing Impellers. *Industrial & Engineering Chemistry Research* 43, 2765-2774.

Roache, P. J. (1994). Perspective: A Method for Uniform Reporting of Grid Refinement Studies. *Journal of Fluids Engineering* 116, 405-413.

Ryma, A., H. Dhaouadi, H. Mhiri and P. Bournot (2013). CFD Study of Turbine Submergence Effects on Aeration of a Stirred Tank. *International Journal of Chemical & Molecular Engineering* 7(4), 173-178.

Wu, H. and G. K. Patterson (1989). Laser-Doppler Measurements of Turbulent Flow Parameters in a Stirred Mixer. *Chemical Engineering Science* 44(10), 2207-2221.

Yapici, K., B. Karasozen, M. Schafer and Y. Uludag (2008). Numerical investigation of the effect of the Rushton type turbine design factors on agitated tank flow characteristics. *Chemical Engineering Proceedings* 47, 1340-1349.

Yianneskis, M., Z. Popiolek and J. H. Whitelaw (1987). An experimental study of the steady and unsteady flow characteristics of stirred reactors. *Journal of Fluid Mechanics* 175, 537-555.

Zamiri, A. and J. T. Chung (2018). Numerical evaluation of turbulent flow structures in a stirred tank with a Rushton turbine based on scale-adaptive simulation. *Computers and Fluids* 170, 236-248.

Zhang, Y., Z. Gao and Z. Li (2017). Transitional Flow in a Rushton Turbine Stirred Tank. *AIChE Journal* 63(8), 3610-3623.

Zhu, Q., H. Xiao, A. Chen, S. Geng and Q. Huang (2019). CFD study on double- to single-loop flow pattern transition and its influence on macro mixing efficiency in fully baffled tank stirred by a Rushton turbine. *Chinese Journal of Chemical Engineering* 27, 993-1000.